OPEN

NPG Asia Materials (2014) 6, e100; doi:10.1038/am.2014.21

www.nature.com/am

REVIEW

Metal oxide mesocrystals with tailored structures and properties for energy conversion and storage applications

Takashi Tachikawa[1,2] and Tetsuro Majima[1]

Mesocrystals (MCs) are superstructures with a crystallographically ordered alignment of nanoparticles. Owing to their organized structures, MCs posses some unique characteristics such as a high surface area, pore accessibility, and good electronic conductivity and thermal stability; thus, MCs could be beneficial for many areas of research and application. This review begins with a description of the common synthesis strategies for, and characterization and fundamental properties of metal oxide MCs. Newly developed analytical methods (that is, photoconductive atomic force microscopy and single-molecule, single-particle fluorescence microscopy) for unraveling the charge transport and photocatalytic properties of individual MCs are then introduced. Further, recent developments in the applications of various metal oxide MCs, especially in the fields of energy conversion and storage, are also reviewed. Finally, several perspectives in terms of future research on MCs are highlighted.
NPG Asia Materials (2014) **6,** e100; doi:10.1038/am.2014.21; published online 16 May 2014

Keywords: energy storage; mesocrystal; metal oxide; photocatalysis; solar energy conversion; superstructure

INTRODUCTION

The self-assembly of nanoparticle building blocks into highly ordered superstructures is one of the actively pursued research topics in materials science and technology.[1–4] Such hierarchical architectures have potentially tunable electronic, optical and magnetic properties, which promise various applications ranging from catalysis to optoelectronics. A mesocrystal (MC), which was first introduced by Cölfen in the early years of 2000s, is defined as a superstructure consisting of nanoparticles on the scale of several hundred nanometers to micrometers.[5–11] In contrast to the classical mechanism of atom/ion-mediated growth of a single crystal, the particle-mediated growth mechanisms of MCs are termed as non-classical crystallization (Figure 1). This definition has been developed in recent years, where MCs are defined entirely according to their structures rather than their formation mechanism.[12] In this decade, a variety of MCs of metal oxides (for example, TiO_2,[13–23] ZnO,[24–34] hematite (α-Fe_2O_3),[35–40] maghemite (γ-Fe_2O_3),[41] Co_3O_4,[42] SnO,[43–45] Ag_2O,[46] CuO[47–49]), metal chalcogenides (for example, ZnS,[50,51] PbS,[52] PbSe[53,54]), metals (for example, Au,[55] Ag,[56,57] Cu,[58] Pt,[59,60] Pd[61]), organic compounds (for example, DL-alanine,[62,63] DL-lysine · HCl,[64] perylene derivatives[65]) and biominerals (for example, sea urchin spines, corals, egg shells)[66] have been synthesized or discovered in nature.

Among metal oxides, TiO_2 is used in many applications that deal with environmental and energy problems (for example, photodegradation of pollutants,[67] water splitting for H_2 evolution,[68] dye-sensitized solar cells[68] and lithium-ion batteries[69]) owing to its chemical stability as well as its low cost and non-toxicity. When TiO_2 is illuminated with ultraviolet (UV) light, electron–hole pairs are created simultaneously. Only a small part of the photogenerated charge carriers spatially separate via diffusion and facilitate surface reactions to generate reactive species (for example, $O_2^{\bullet -}$ and $^{\bullet}OH$) for subsequent oxidation/reduction processes on TiO_2 surfaces.[70] Thus, highly active photocatalysts require high charge separation efficiency in addition to a high specific surface area for the adsorption of reagents. Controlled crystal growth also determines the exposed facets of crystals as well as their shape and size, which have different surface physicochemical properties.[71,72] As Yang *et al.*[73] successfully synthesized anatase TiO_2 single crystals with highly exposed reactive {001} facets, enormous efforts have been devoted to the synthesis of anatase TiO_2 crystals with different crystal planes exposed for better performance.[74] Furthermore, mesoporous TiO_2 single crystals with well-defined facets have been prepared and utilized in dye-sensitized solar cells and photocatalysis for H_2 evolution and degradation of dyes.[75,76]

It has been suggested that the dense packing of TiO_2 nanocrystals (NCs) enhances the photocatalytic activity and performance of dye-sensitized solar cells owing to the efficient interparticle electron transfer between NCs.[77–83] For example, the Choi group reported that mesoporous TiO_2 consisting of compactly packed nanoparticles showed higher photocatalytic activity for H_2 evolution than that shown by colloidal and commercial TiO_2 samples in both UV and visible light (dye-sensitized) systems.[78] In addition, transient

[1]The Institute of Scientific and Industrial Research (SANKEN), Osaka University, Osaka, Japan and [2]PRESTO, Japan Science and Technology Agency (JST), Saitama, Japan
Correspondence: Professor T Majima, The Institute of Scientific and Industrial Research (SANKEN), Osaka University, Mihogaoka 8-1, Ibaraki, Osaka 567-0047, Japan.
E-mail: tachi45@sanken.osaka-u.ac.jp or majima@sanken.osaka-u.ac.jp
Received 1 December 2013; revised 14 January 2014; accepted 4 February 2014

photocurrent measurements and random walk numerical simulations have shown that the ordering of a nanocrystalline structure significantly influences charge transport and recombination, which are closely related to the performance of photovoltaic cells.[82,83] Zaban and co-workers[82] found that the highest degree of ordering in porous TiO_2 nanocrystalline films correlates with the highest values of effective diffusion coefficient. Indeed, MCs consisting of NCs highly oriented in the same direction are an ideal system to study this issue.

In this review, we focus on the synthesis and structures of metal oxide MCs, mostly TiO_2 MCs, and their applications for energy conversion and storage. We selected examples, which showed the most marked enhancement of physical properties in applications. For instance, owing to their high specific surface area and mesoporous structures, TiO_2 MCs could show higher photocatalytic activity for H_2 evolution and organics degradation than that shown by bulk single crystals. The higher photocatalytic activity of TiO_2 MCs is strongly related to the facile interparticle electron transport between NCs in the MC superstructure. Finally, we summarize our contribution together with some future research directions in various aspects.

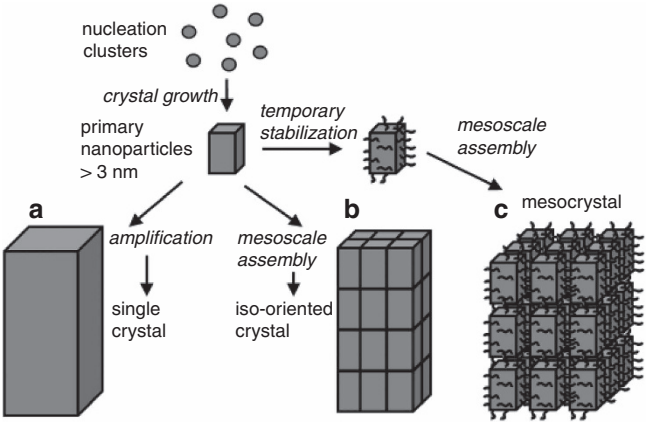

Figure 1 Schematic illustration of classical and non-classical crystallization. (**a**) Classical crystallization pathway, (**b**) oriented attachment of primary nanoparticles forming an iso-oriented crystal upon fusing, (**c**) mesocrystal (MC) formation via self-assembly of primary nanoparticles covered with organics. Reprinted with permission from reference Wohlrab *et al.*[62] Copyright 2005 WILEY-VCH Verlag GmbH & Co. KGaA, Weinheim.

SYNTHESIS OF MCS

In this section, we briefly overview the synthesis of metal oxide MCs by several different approaches. As the details of the synthesis procedures for and formation mechanisms of MCs are beyond the scope of this article, we request interested readers to refer to the comprehensive reviews cited in Introduction section.[6–11]

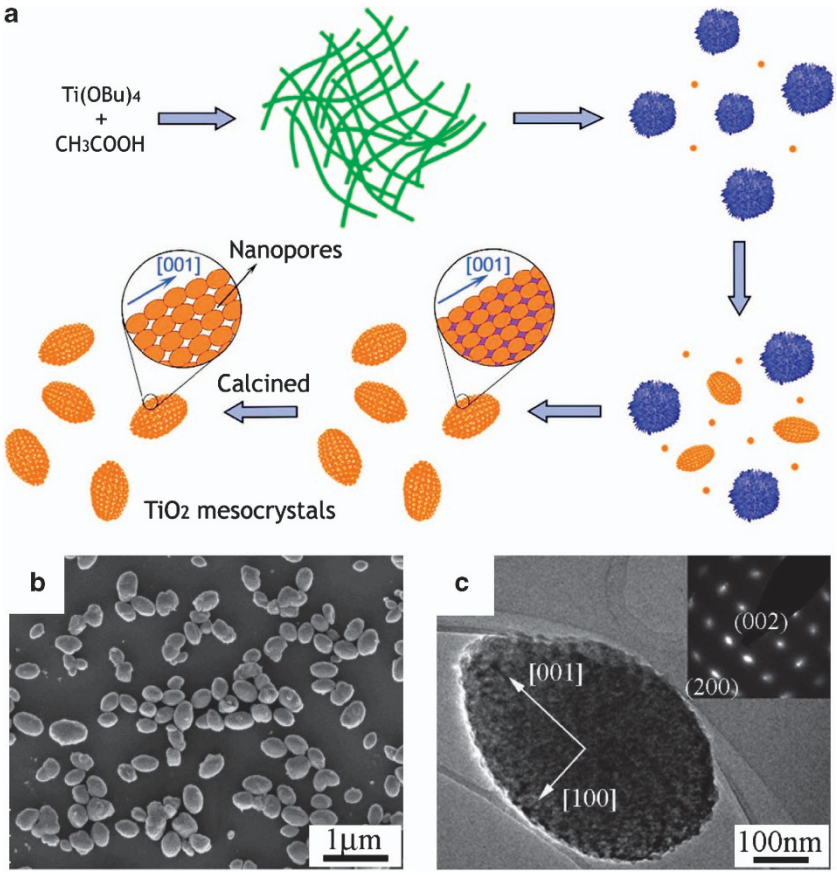

Figure 2 (**a**) Schematic illustration of the formation of spindle-shaped anatase TiO_2 mesocrystals (MCs). (**b**) Scanning electron microscopy (SEM) and (**c**) transmission electron microscopy (TEM) images of TiO_2 MCs. Reprinted with permission from reference Ye *et al.*[16] Copyright 2011 American Chemical Society.

The method most commonly used to synthesize MC materials is based on hydrothermal/solvothermal treatments in which a solution is maintained at a specific temperature and aged for a specific period of time. The resulting precipitates are then collected and washed to remove impurities. In some cases, the precipitates require further annealing. For example, the Qi group synthesized spindle-shaped anatase TiO_2 MCs by the solvothermal treatment of a solution of tetrabutyl titanate in acetic acid and subsequent calcinations. As illustrated in Figure 2a, the reaction between tetrabutyl titanate and acetic acid first forms unstable titanium acetate complexes by ligand exchange/substitution, concomitant with the release of butanol.[16] The concomitant Ti–O–Ti condensation forms transient amorphous fiber-like precursors. Flower-like precursors are then produced at the expense of the transient precursors and release soluble titanium-containing species for the nucleation and growth of anatase NCs. These NCs undergo oriented aggregation along the [001] direction, consequently resulting in the formation of spindle-shaped anatase MCs (Figures 2b and c). The Brunauer–Emmett–Teller surface area and pore volume of the synthesized TiO_2 MCs were $114\,m^2\,g^{-1}$ and $0.14\,m^3\,g^{-1}$, respectively. Further, using the solvothermal method, Li and co-workers[17] synthesized single crystal-like anatase TiO_2 MCs with a high surface area of $180\,m^2\,g^{-1}$ and a uniform pore diameter of 3.4 nm. These TiO_2 MCs had either massive or granular structures in which most of the high-energy {001}surfaces were hidden in the bulk.

The O'Brien group were the first to prepare anatase TiO_2 MCs via the topotactic transformation of NH_4TiOF_3 crystals.[13] The topotactic transformation is a solid-state transformation in which the final product is structurally and orientationally related to the starting material. Figure 3 illustrates the topotactic transformation of NH_4TiOF_3 to anatase TiO_2 MC. As the structures of NH_4TiOF_3 and anatase TiO_2 are very similar, the positions of Ti atoms in the {001} planes are well matched with each other. Using a similar synthesis strategy, Yu *et al.*[19] synthesized layered anatase TiO_2 nanosheets with exposed {001} facets by a simple hydrothermal method, followed by calcination.

In 2012, Bian *et al.*[21] significantly improved the synthesis method for anatase TiO_2 MCs with dominant {001} facets. Their improved method is illustrated in Figure 4a; plate-like TiO_2 MCs are obtained by annealing a thin layer of an aqueous solution containing TiF_4, NH_4F and NH_4NO_3 (without surfactants) on a silicon wafer. In this one-step annealing process, the material undergoes changes in two stages. First, the precursors of Ti^{4+}, F^-, NH^{4+} and H_2O begin a series of combination reactions during evaporation of water at low temperatures to form NH_4TiOF_3. With further increase in annealing temperature, NH_4TiOF_3 is topotactically transformed into anatase TiO_2. When large amounts of N, H and F atoms are removed, the volume of nanoparticles decreases and gaps or pores are formed between nanoparticles, resulting in the formation of porous TiO_2

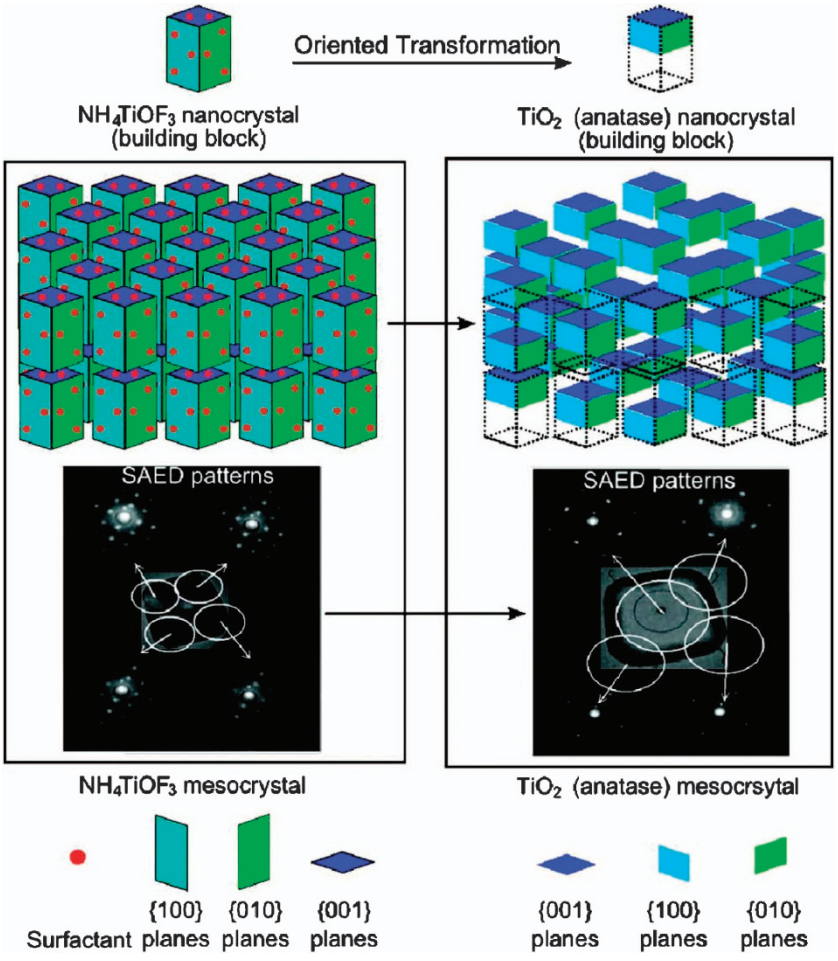

Figure 3 Schematic illustration of the topotactic transformation of NH_4TiOF_3 to anatase TiO_2 mesocrystal (MC). Reprinted with permission from reference Zhou *et al.*[13] Copyright 2008 American Chemical Society.

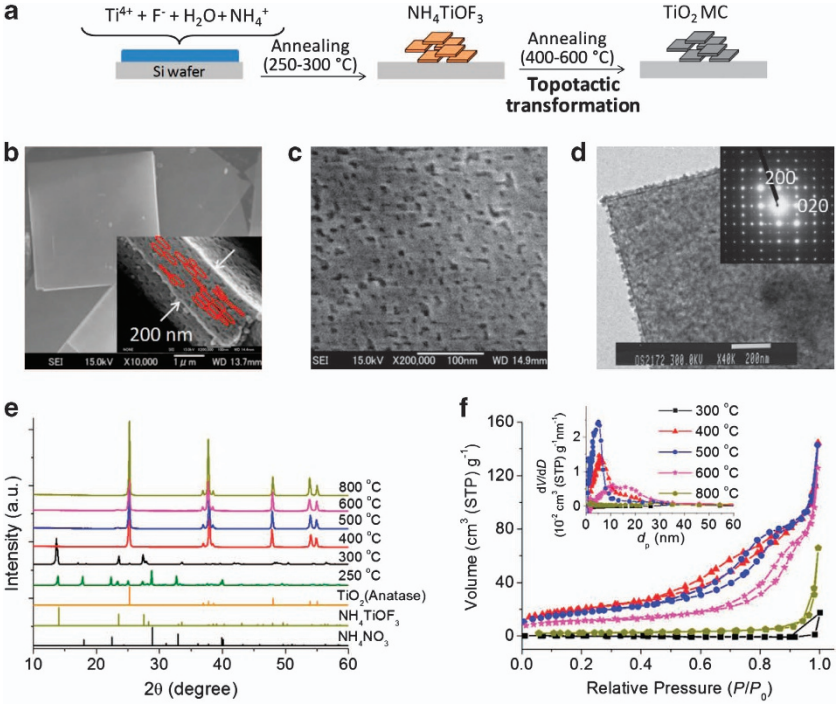

Figure 4 (**a**) Formation of NH_4TiOF_3 at low annealing temperatures (250–300 °C) and topotactic transformation from NH_4TiOF_3 to TiO_2 mesocrystals (MCs) at higher annealing temperatures. (**b**) Scanning electron microscopy (SEM) images of TiO_2 MCs annealed at 500 °C showing a plate-like morphology. Inset shows assembled nanocrystals (NCs) on the lateral surface of TiO_2 MC. (**c**) Magnified SEM image of a crystal surface revealing a porous structure. (**d**) Transmission electron microscopy (TEM) image of a representative crystal showing a mesoporous structure, and selected-area electron diffraction (SAED) pattern (inset) showing single-crystal diffraction along the anatase [001] zone axis. (**e**) X-ray diffraction (XRD) patterns and (**f**) N_2 adsorption–desorption isotherms and pore size distribution (inset) of the products obtained at different annealing temperatures. Reprinted with permission from reference Bian *et al.*[21] Copyright 2012 American Chemical Society.

MCs that consist of anatase single-crystalline nanoparticles with the {001} surfaces as dominant facets.

They characterized the structures of the synthesized TiO_2 MCs by scanning electron microscopy (SEM) and transmission electron microscopy. The TiO_2 MCs showed a plate-like structure several micrometers in size and 50–300 nm in thickness (Figure 4b). The MCs were composed of an ordered alignment of anatase TiO_2 NCs with an average size of approximately 40 nm. A porous structure with pore diameters of several nanometers was confirmed by high-resolution scanning electron microscopy and transmission electron microscopy images (Figures 4c and d). It is worth mentioning here that a selected-area electron diffraction pattern of the crystal (inset) corresponded to single-crystal anatase along the [001] zone axis, thus suggesting the formation of anatase TiO_2 with the {001} facet exposed. An oriented arrangement of NCs decreases the grain boundaries in a sample. The pure phase of anatase was thus retained after calcination at 800 °C. The enhanced phase stability was explained by the assumption that the transformation to the rutile phase was inhibited by the elimination of interfacial nucleation sites.[16]

To understand the formation mechanism of anatase TiO_2 MCs, they compared the scanning electron microscopy images, X-ray diffraction patterns, N_2 adsorption–desorption isotherms and pore size distribution of the samples obtained at different synthesis temperatures (Figures 4e and f). NH_4TiOF_3 growth started at 250 °C with a mixture NH_4TiOF_3 and NH_4NO_3 during the evaporation of water (Figure 4e). Pure NH_4TiOF_3 with a plate-like structure was observed at 300 °C, but it did not have any pore structure on the surface and its specific surface area was very low ($\sim 0.4\,m^2\,g^{-1}$) (Figure 4f). After annealing at 400 °C, the obtained product was pure anatase TiO_2 (Figure 4e) and had a porous structure with a specific surface area of $74\,m^2\,g^{-1}$ and a pore size of approximately 5 nm. Furthermore, no apparent change in morphology was observed, indicating the topotactic transformation from NH_4TiOF_3 to TiO_2 by the removal of N, H and F atoms from the crystal lattice. This removal of atoms resulted in the creation of space between TiO_2 NCs, and thus, a porous structure was formed in the crystal. Upon further increasing the calcination temperature, the morphology and crystalline phase of TiO_2 remained unchanged, while the mutual fusion of NCs led to an increase in the particle size, a decrease in the specific surface area and an increase in the pore size (Figure 4f).

Another important progress is the formation of MCs *via* electrochemical deposition.[46,49] For example, Fang *et al.*[46] reported an external electric field-driven particle-mediated bottom-up approach for synthesis of Ag_2O MCs with different morphologies. Figure 5 shows the scanning electron microscopy images of the as-prepared Ag_2O MCs under different applied potentials and growth times. The morphologies of the products obtained under different conditions are remarkably different (rhombic hexahedron, cube and dodecahedron), and the rough surface of MCs reveals a nonclassical crystallization process (insets of Figure 5).

An external magnetic field has also been applied to induce the self-assembly of γ-Fe_2O_3 nanocubes into micrometer-sized MC structures.[41] The thickness of the MCs is controllable by varying the concentration of the nanoparticle dispersion as well as the duration of the applied magnetic field.

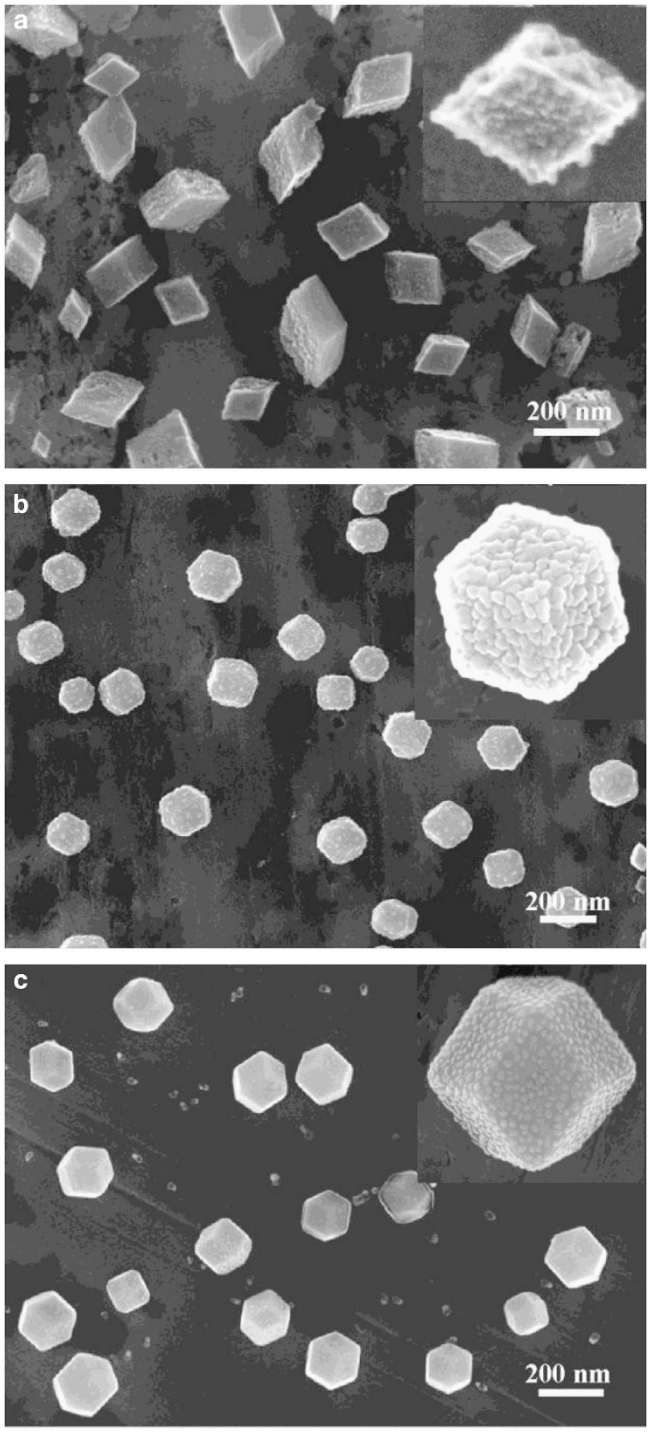

Figure 5 Scanning electron microscopy (SEM) images of Ag_2O mesocrystals (MCs) synthesized at silver ion concentration of 1 mM, applied potential and growth time of (**a**) 30 V and 3 min, (**b**) 15 V and 3 min and (**c**) 5 V and 5 min. Reprinted with permission from reference Fang *et al.*[46] Copyright 2010 Elsevier BV.

OPTICAL PROPERTIES OF MCS

MCs are expected to exhibit some interesting and unique optical properties owing to their structural features. Wu *et al.*[26] synthesized core-shell-structured ZnO MC microspheres by a hydrothermal method in the presence of a water-soluble polymer. The whole surface of these MCs was composed of densely packed ZnO nanoplatelets aligned perpendicularly to the microspheres. Interestingly, these ZnO MCs exhibited strong mechanical resonance and radiative emission at ~0.36 THz under 514.5-nm continuous-wave laser irradiation. This property originated from the laser-induced coherent vibration of the ZnO nanoplatelets.

Hu *et al.*[84] demonstrated that $AgIn(WO_4)_2$ MCs exhibit a white emission in the visible region when excited by 460-nm light. Their photoluminescence (PL) strongly correlated with the surface nanostructures of outgrowths; a larger amount of outgrowths led to stronger emission intensities. The MCs with high surface-to-volume ratios had more surface defects, which were responsible for the radiative recombination of charge carriers. In addition, Li *et al.*[24] found that the PL properties of hollow-type ZnO MCs are largely governed by the number and nature of defects in the ZnO lattice.

Bian *et al.*[85] investigated the recombination of photogenerated electrons and holes in plate-like TiO_2 MCs that yields distinct PL in the visible region. Figure 6a shows a typical emission image acquired for two partially overlapping TiO_2 MCs during 380-nm photoexcitation in ambient air. Spectral measurements revealed a broad emission band at the center positions of the crystal at around 450–600 nm (Figure 6b), which originated from surface states.[86,87] The average PL lifetimes of TiO_2 MCs and NCs were around 5.9 and 2.0 ns, respectively (Figure 6c). Shorter (longer) PL lifetime of the samples indicates relatively faster (slower) charge recombination. Thus, it was concluded that the MC superstructure significantly improved charge separation efficiency. They also found that the average lifetime measured at the center of the MCs (5.5 ns) was slightly shorter than that measured at their edge (6.9 ns). The location-dependent nature of PL implied that charges trapped near the edge were subjected to a different recombination probability as compared with those trapped at the center.

ELECTRON TRANSPORT IN MC

Experiments on a single assembly of NCs revealed the superior physicochemical properties of ordered superstructures that are unattainable using conventional disordered systems. To explore the intricate relationship between structure and function, Bian *et al.*[21] investigated the photoconductivity of individual TiO_2 MCs by means of conductive atomic force microscopy, with the instrument equipped with a UV light source (Figure 7a). As shown in Figures 7b, a significant photocurrent response was observed in case of UV irradiation on a single plate-like TiO_2 MC on an indium tin oxide electrode, while there was no measurable current response without UV irradiation. From the thickness dependence of the photocurrent, the photoconductivity was calculated to be $2 \times 10^{-2}\,\Omega^{-1}\,m^{-1}$ in air, which was several orders greater than that of aggregated TiO_2 NCs with a similar size (~200 nm) under the same conditions (Figure 7b). This result suggested that electron transport ability in TiO_2 MCs was largely improved possibly because of the intimate contact between NCs and/or between NCs and electrodes.

Single-molecule, single-particle fluorescence micro(spectro)scopy has emerged as a powerful tool for obtaining information about the structure and dynamics of individual objects.[88,89] Bian *et al.*[85] applied this technique to determine the location of reactive sites on plate-like TiO_2 MCs by using a redox-responsive fluorogenic probe. By accepting electrons from photoexcited TiO_2, nonfluorescent 8-(3,4-dinitrophenyl)-1,3,5,7-tetramethyl-4,4-difluoro-4-bora-3*a*,4*a*-diaza-*s*-indacene (DN-BODIPY; fluorescence quantum yield $\Phi_{fl} < 10^{-4}$ in methanol) was reduced to form highly fluorescent 4-hydroxyamino-3-nitrophenyl-BODIPY (HN-BODIPY; $\Phi_{fl} = 0.50$ in methanol)

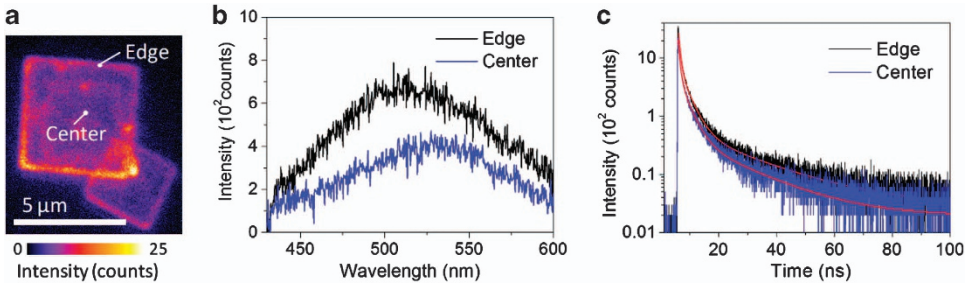

Figure 6 (**a**) Photoluminescence (PL) image of TiO_2 mesocrystals (MCs) immobilized on a quartz glass (excitation wavelength: 380 nm). (**b**) PL spectra and (**c**) decay profiles observed at the center and edge positions on TiO_2 MCs. The red curves indicate multiexponential curves fitted to the kinetic trace. Reprinted with permission from reference Bian *et al.*[85] Copyright 2012 American Chemical Society.

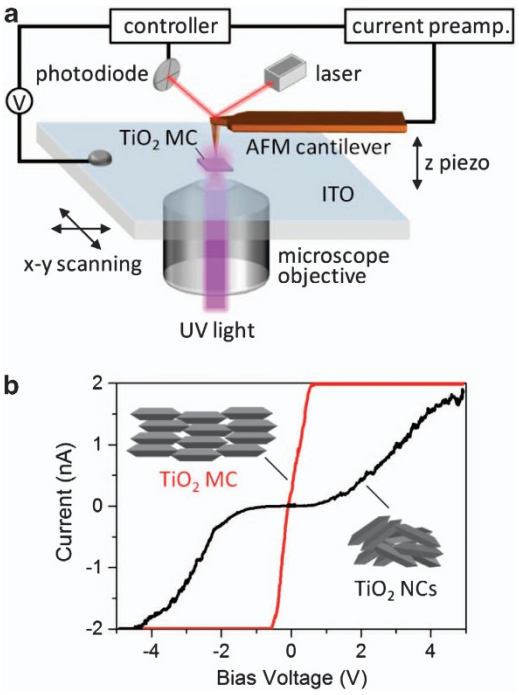

Figure 7 (**a**) A schematic of photoconductive atomic force microscopy (AFM). The platinum AFM tip was used to measure the surface topography and photocurrent under bias potential. The ultraviolet (UV) light is focused on the device through the indium tin oxide (ITO)-coated cover glass using an inverted fluorescence microscope. (**b**) Typical current–voltage curves measured for TiO_2 mesocrystal (MC) (red) and aggregated TiO_2 NCs (black) at constant UV intensity (9 mW cm^{-2}). Reprinted with permission from reference Bian *et al.*[21] Copyright 2012 American Chemical Society.

(Figure 8a). The locations of the reduction sites were determined via centroid analysis of each fluorescent spot obtained for individual MCs. As shown in Figures 8b and c, most of the fluorescence spots, that is, catalytically active sites, were found to be located near the edges of the MCs. This interesting finding was consistent with the observation that Au and Pt nanoparticles were preferentially photodeposited at the edges of TiO_2 MCs with {101} facets (Figures 8e and f). In addition, the average rate of the formation of fluorescent products on the basal surfaces decreased from 5.6 to 2.3 molecules μm^{-2} s^{-1} upon Au loading on TiO_2 MCs, whereas the reaction rate on the lateral surfaces increased from 11 to 19 molecules μm^{-2} s^{-1} (Figure 8d). These differences strongly supported the mechanism in which photogenerated electrons on the basal surfaces of TiO_2 MCs can rapidly migrate to Au nanoparticles loaded on the lateral surfaces through the NC network. This anisotropic electron transport greatly improved the photocatalytic performance to be better than that of conventional disordered systems (Figures 8g and h). In fact, the metal-nanoparticle-loaded TiO_2 MC composites exhibited higher photocatalytic activity than the NC-based composites. Further, the loading amounts of noble metals required to achieve 50% of the photocatalytic degradation of 4-chlorophenol were compared under the same experimental conditions. The optimum loading amounts of metals on TiO_2 MCs (for example, 0.04 and 0.2 wt% for Au and Pt, respectively) were about 10 times lower than those on TiO_2 NCs (for example, 0.4 and 4.0 wt% for Au and Pt, respectively). This is desirable for the practical use of TiO_2 MCs as photocatalysts because of the high price of noble metals.

LITHIUM STORAGE PROPERTIES OF MCS

MCs can be used in Li-ion batteries as either anode or cathode materials. The MC structure provides not only facile electronic conduction but also fast Li ion transport between the MC electrode and electrolyte. For example, Ye *et al.*[16] prepared anatase TiO_2 MCs (see Figure 2) and used them as an anode material for a high-power Li-ion battery. As shown in Figure 9, the MC electrode exhibited better rate capability than a TiO_2 nanoparticle electrode at high current rates. The uniformly porous structure of MCs facilitated their contact with the electrolyte and hence was also advantageous for fast Li-ion transport. The TiO_2 MCs delivered specific discharge capacities of 164.9 and 151.7 mA h g^{-1} at 1 and 2 °C, respectively; these values were larger than those reported for TiO_2 hollow spheres and were comparable with those reported for mesoporous spheres.

Duan *et al.*[40] prepared high-stability α-Fe_2O_3 MCs by a facile solvothermal method without polymer additives, and evaluated the discharge cycling performance of an electrode fabricated using α-Fe_2O_3 MCs with different morphologies. Rhombic α-Fe_2O_3 MCs showed the best cycling stability owing to closed and intracrystalline porosity.

PHOTOCATALYTIC PERFORMANCE OF MCS

The design and preparation of mesoporous TiO_2 photocatalysts have attracted increasing interest in recent years owing to their exceptional properties and widespread potential applications. Tartaj[18] synthesized anatase TiO_2 MCs that exhibited good photocatalytic activity for organics degradation under UV light irradiation owing to their high crystallinity. Owing to their unique structural features, TiO_2 MCs

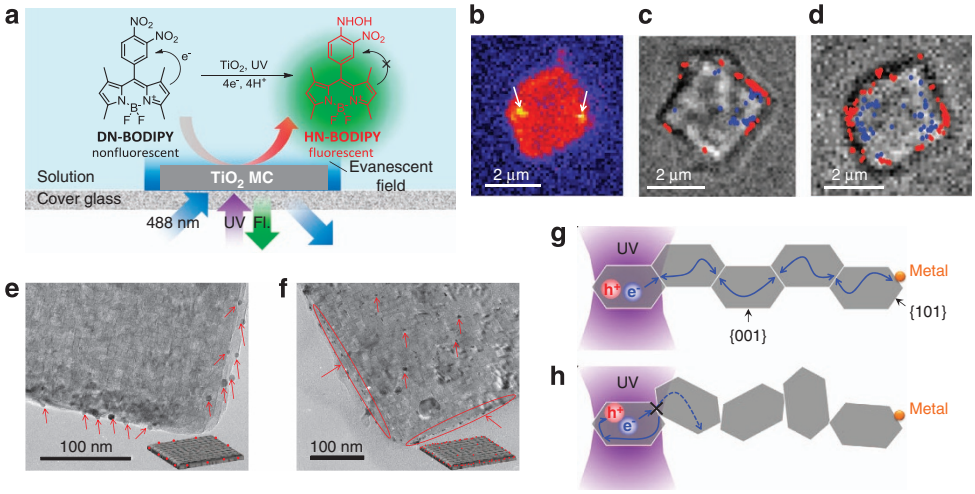

Figure 8 (**a**) Single-molecule fluorescence observation of photocatalytically generated fluorescent 4-hydroxyamino-3-nitrophenyl-BODIPY (HN-BODIPY) from nonfluorescent 8-(3,4-dinitrophenyl)-1,3,5,7-tetramethyl-4,4-difluoro-4-bora-3*a*,4*a*-diaza-*s*-indacene (DN-BODIPY) under ultraviolet (UV) light irradiation by total internal reflection fluorescence microscopy. (**b**) Fluorescence image of a 0.04 wt% Au/TiO_2 mesocrystal (MC) particle immobilized on a cover glass in Ar-saturated DN-BODIPY solution (0.5 μM in methanol) under 488-nm laser (0.1 kW cm^{-2}) and UV light irradiation (30 mW cm^{-2}). The arrows denote the locations of fluorescence spots. Optical transmission images of (**c**) TiO_2 MC and (**d**) 0.04 wt% Au/TiO_2 MC immobilized on a cover glass. The blue and red dots indicate the location of fluorescence bursts on the basal and lateral surfaces of the crystal, observed during 15 s of irradiation. Transmission electron microscopy (TEM) images of a representative crystal of (**e**) 0.04 wt% Au/TiO_2 MC and (**f**) 1.0 wt% Pt/TiO_2 MC. Schematic illustration of electron transport processes in (**g**) structurally ordered MC and (**h**) disordered nanocrystal (NC) aggregation. The symbols e^- and h^+ indicate photogenerated electrons and holes, respectively. Reprinted with permission from reference Bian *et al.*[85] Copyright 2012 American Chemical Society.

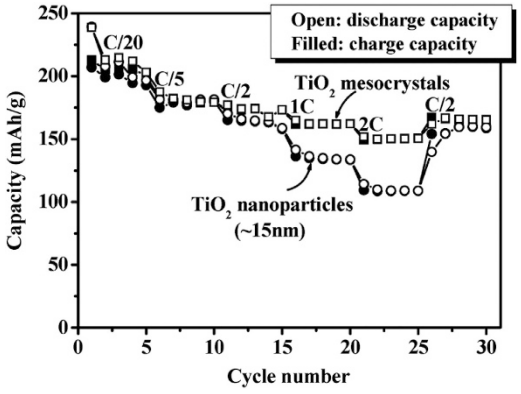

Figure 9 Rate capability of TiO_2 mesocrystals (MCs) and nanoparticles from C/20 to 2C (1C = 170 mA g^{-1}) for five cycles. Reprinted with permission from reference Ye *et al.*[16] Copyright 2011 American Chemical Society.

maintain a large specific surface area along with their good crystallinity.

Yu *et al.* prepared rutile TiO_2 MCs by a microwave-assisted hydrothermal method.[15] The TiO_2 MCs are composed of rutile nanowires with an average aspect ratio of approximately 270. These MCs showed good photocatalytic activity and stability for NO removal under UV or simulated solar light irradiation. Au modification of these TiO_2 MCs led to a 50% improvement in their photocatalytic performance. The researchers ascribed the high photocatalytic ability to the following factors: (i) a high aspect ratio of the rutile TiO_2 nanowires that allowed fast charge transport; (ii) a large effective surface area of the TiO_2 MCs that resulted in easier diffusive transport of photogenerated holes to the target molecules; and (iii) efficient penetration of light and diffusion of NO molecules into the photocatalyst because of open pores.

The above-mentioned plate-like TiO_2 MCs exhibited decent performance for the photocatalytic oxidation of 4-chlorophenol and rhodamine B as well as for the photocatalytic reduction of Cr^{6+} in water.[21] The photocatalytic activities of these TiO_2 MCs exhibited a 100–300% enhancement relative to that of anatase TiO_2 NCs with dominant {001} facets and a similar specific surface area; the observed marked enhancement in activity could not be attributed to the specific surface area of the NCs. The photocatalytic performance of the TiO_2 MCs was nearly similar to that of benchmark P25 TiO_2 (Figures 10a–c). Time-resolved diffuse reflectance spectroscopy was used to directly measure the lifetime of a charge-separated state; this measure is a criterion for evaluating the efficiency of photocatalytic reactions.[70] As shown in Figure 10d, the TiO_2 MCs exhibited a broad transient absorption band in the visible to near-infrared range upon 355-nm laser excitation, which represented the overlapping of trapped holes (mainly 440–600 nm) and trapped electrons (mainly 660–900 nm).[70] 4-(Methylthio)phenyl methanol (MTPM) was then selected as the probe molecule to estimate the lifetime of the charge-separated state.[70] As can be clearly seen in Figure 10e, the 550-nm absorption band of the MTPM radical cation ($MTPM^{\bullet+}$) was indicative of one-electron oxidation of adsorbed MTPM by photogenerated holes. The half-lives of $MTPM^{\bullet+}$ were determined to be ~2 μs for the TiO_2 MC systems, which was much longer than that of TiO_2 NC (~0.5 μs). Hence, TiO_2 MCs could exhibit greatly increased photocatalytic activity owing to their superstructure that enhances charge separation.

Another interesting example is that of anatase TiO_2 MCs with different proportion of {001} and {101} facets synthesized by Chen *et al.*[22] The proportion of {101} facets was tuned by adjusting the solvothermal periods. As shown in Figure 11, the TiO_2 MCs with a high proportion of {101} facets possessed higher photooxidation/reduction activity than those with a lower proportion. This result was explained in terms of the synergistic effect of Ti^{3+} and the proportion of {101} facets. In addition, the normalized photocatalytic activity of

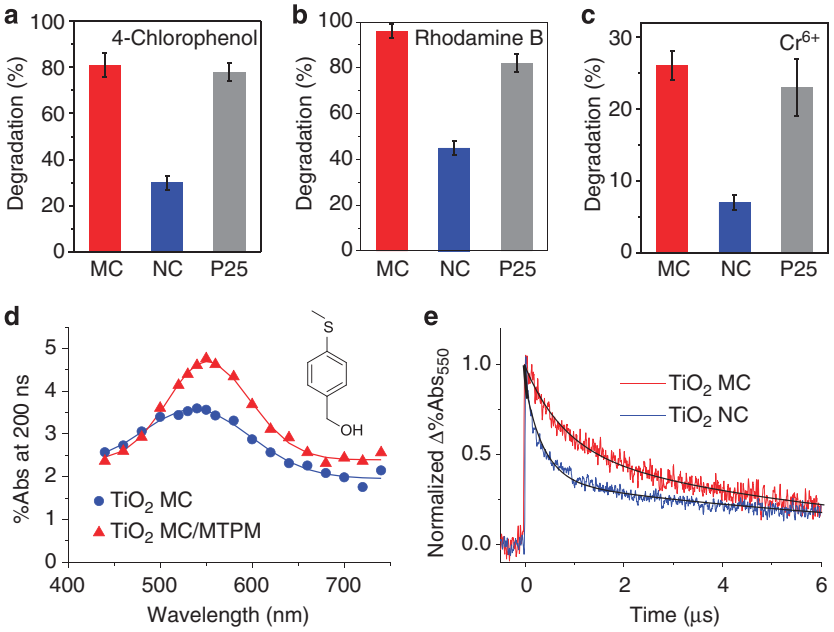

Figure 10 Photocatalytic degradation of (**a**) 4-chlorophenol, (**b**) rhodamine B and (**c**) Cr^{6+} in aqueous phase in the presence of different TiO_2 samples. (**d**) Time-resolved diffuse reflectance spectra observed at 200 ns after a laser flash during the 355-nm laser flash photolysis of TiO_2 mesocrystal (MC) in the absence and presence of 4-(methylthio)phenyl methanol (MTPM; 10 mM) in acetonitrile. The inset indicates the molecular structure of MTPM. The absorption peak at around 550 nm is assigned to $MTPM^{\bullet+}$. (**e**) Differential time traces of %Abs at 550 nm obtained by subtracting the time trace observed in the absence of MTPM from that observed in the presence of MTPM (10 mM) for different TiO_2 samples in acetonitrile. Reprinted with permission from reference Bian *et al.*[21] Copyright 2012 American Chemical Society.

TiO_2 MCs was higher than that of TiO_2 nanopolycrystals when the proportion of {101} facets was equal; this indicated that the structural integrity of the crystals had a key role in determining the photocatalytic activity. Liu and co-workers[90] synthesized hollow-type anatase TiO_2 MCs with dominant {101} facets via a new route by using PO_4^{3-}/F^- as morphology-controlling agents. The hollow MCs were more active in H_2 evolution from water splitting and CH_4 generation from photoreduction of CO_2, but were less active in O_2 evolution from water splitting than hollow single crystals with a similar surface area. Interestingly, this reaction preference could be attributed to the fact that the hollow MCs had higher conduction and valence band edges than the hollow single crystals.

MC-BASED COMPOSITE MATERIALS

The direct growth method using topotactic transformation is suitable for constructing MC assemblies or layers on a variety of support materials. In 2008, Liu and Zeng[91] developed a mild one-pot solution approach to prepare anatase TiO_2 MCs on multiwalled carbon nanotubes (CNTs) with controllable surface coverage, surface area, crystal orientation and TiO_2/CNTs ratio. CNTs were mixed with a TiF_4 aqueous solution and held over an ultrasonic water bath for 30 min. The subsequent aging at 60 °C for 20 h produced CNTs covered with closely arranged TiO_2 crystallites with sizes in the range 2–4 nm (Figures 12a and b). The as-prepared TiO_2/CNTs nanocomposites showed better performance for photocatalytic degradation of an organic dye than P25 and CNTs because of (i) the high specific surface area that provided abundant adsorption sites for reactants; (ii) the porous structure that allowed efficient transport of reactants and products; (iii) the oriented arrangement of TiO_2 NCs that minimized light reflections and allowed light transmission to deeper parts of the catalyst; and (iv) surface defect sites and conductive CNTs support

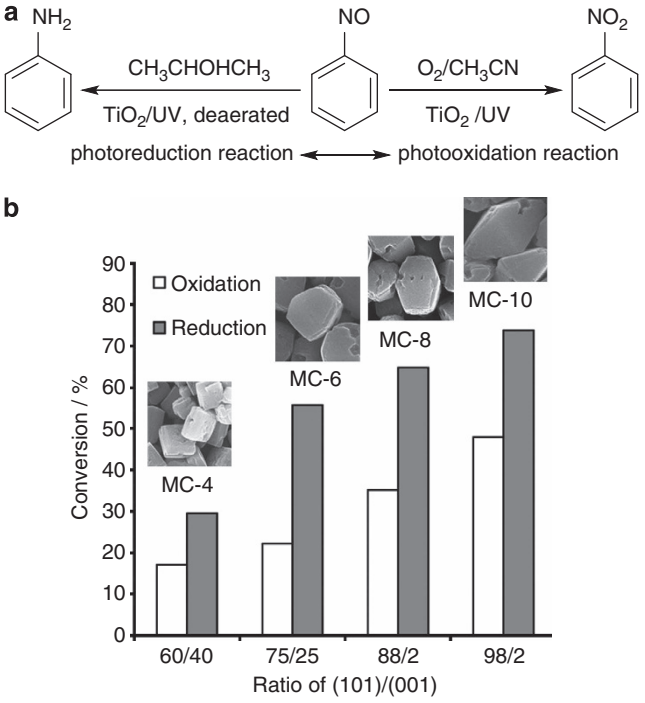

Figure 11 (**a**) Photocatalytic reduction and oxidation reaction of nitrosobenzene under different conditions. (**b**) Photocatalytic activity of different TiO_2 mesocrystals (MCs) with various proportions of (001) and (101) facets. The inset shows scanning electron microscopy (SEM) images of the sample (image size: 1×1 μm). Reprinted with permission from reference Chen *et al.*[22] Copyright 2012 WILEY-VCH Verlag GmbH & Co. KGaA, Weinheim.

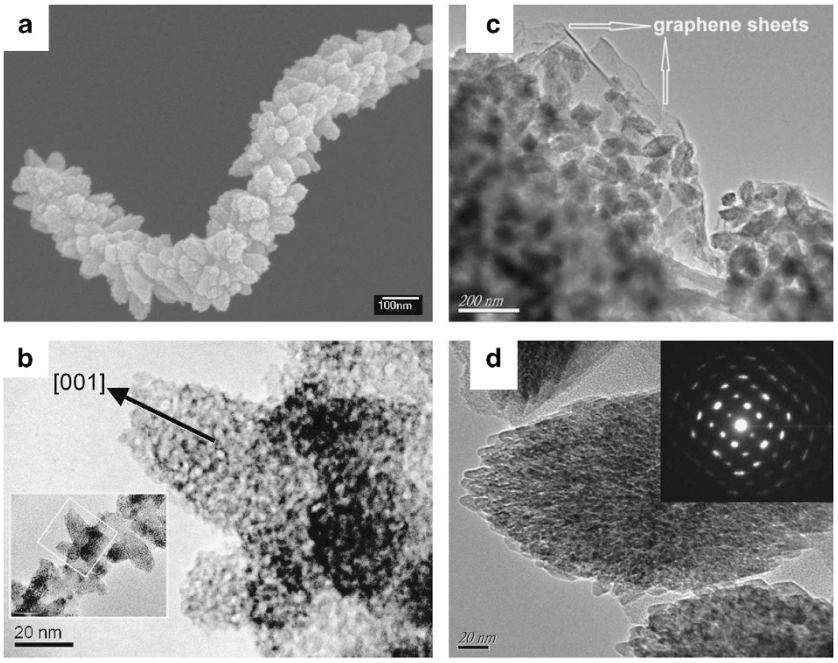

Figure 12 (**a**) Field emission scanning electron microscopy (FESEM) and (**b**) transmission electron microscopy (TEM) image of mesoporous TiO_2/carbon nanotube (CNT) nanocomposites. The examined location is indicated with a frame in the inset image. Reprinted with permission from reference Liu and Zeng[91]. Copyright 2008 American Chemical Society. (**c**, **d**) TEM images of graphene (GR)-TiO_2 composites. Inset in panel (**d**) shows a selected-area electron diffraction (SAED) pattern of the composites. Reprinted with permission from reference Yang *et al.*[92] Copyright 2013 Elsevier BV.

that may have served as electron reservoirs to suppress the recombination of electron–hole pairs. Yang *et al.*[92] prepared graphene-TiO_2 MC composites by a facile template-free process based on a combination of sol–gel and solvothermal methods (Figures 12c and d). The resulting products exhibited a uniform distribution of nanoporous anatase TiO_2 MCs on the graphene sheets. Composites prepared in the presence of different amounts of graphene oxide exhibited higher photocatalytic activity for photocatalytic degradation of rhodamine B than pure TiO_2 MCs and P25.

SUMMARY AND PERSPECTIVES

The focus of current researches in the field of nanoscience and nanotechnology is shifting from the synthesis of individual NCs to the preparation and characterization of their MC superstructures and the realization of their applications. Although self-assembly of NCs by utilizing nanoscale attractive forces provides a simple approach for the fabrication of MCs, the synthesis procedures are sometimes very complicated, and hence, their large-scale applications are limited. A highly reproducible, facile synthesis of MCs with a controlled shape and size is strongly desirable for fundamental research and practical applications. One of the alternative strategies for fabricating such MCs is top–down fabrication through topotactic transformation.

MCs are also an ideal platform for constructing multifunctional materials that incorporate a variety of functional materials. For instance, the development of composite MCs consisting of two or more different types of metal oxide NCs (for example, composites of p- and n-type semiconductors) opens up exciting new opportunities for designing and constructing much more efficient photocatalysts and photovoltaic devices. Such binary nanoparticle superstructures have been well developed for several metals and chalcogenides but not yet for semiconductor metal oxides.[93–95]

Experiments on a single-particle assembly have revealed that ordered superstructures produce a high yield of photogenerated charges and have high photoconductivity, which are difficult to achieve using traditional disordered systems consisting of crystalline nanoparticles owing to the inevitable occurrence of charge recombination at the internal interface. The Majima group used single-molecule, single-particle fluorescence microscopy to show that photogenerated electrons could reach reactive sites over a micrometer distance and are preferentially trapped at the edge of plate-like TiO_2 MCs, in which {101} facets are predominantly exposed.[21,85] This anisotropic electron transport significantly retarded the charge recombination with holes, thereby resulting in enhanced photocatalytic activity. The excellent charge/molecular transport properties of MCs thus hold great promise for energy conversion and storage applications. Further development of the synthesis methods for MCs and understanding of their fundamental properties will lead to the production of innovative materials with potential applications in energy conversion and storage, catalysis and sensing.

CONFLICT OF INTEREST

The authors declare no conflict of interest.

ACKNOWLEDGEMENTS

TM thanks to the WCU (World Class University) program through the National Research Foundation of Korea funded by the Ministry of Education, Science and Technology (R31-10035) for the support. This work has been partly supported by a Grant-in-Aid for Scientific Research (projects 25220806, 25810114, and others) from the Ministry of Education, Culture, Sports, Science and Technology (MEXT) of the Japanese Government.

1 Caruso, F. (ed.) *Colloids and Colloid Assemblies* (Wiley-VCH, Weinheim, Germany, 2003).
2 Mann, S. Self-assembly and transformation of hybrid nano-objects and nanostructures under equilibrium and non-equilibrium conditions. *Nat. Mater.* **8,** 781–792 (2009).
3 Nie, Z., Petukhova, A. & Kumacheva, E. Properties and emerging applications of self-assembled structures made from inorganic nanoparticles. *Nat. Nanotechnol.* **5,** 15–25 (2010).
4 Liu, J.-W., Liang, H.-W. & Yu, S.-H. Macroscopic-scale assembled nanowire thin films and their functionalities. *Chem. Rev.* **112,** 4770–4799 (2012).
5 Cölfen, H. & Antonietti, M. *Mesocrystals and Nonclassical Crystallization* (Wiley, West Sussex, England, 2008).
6 Cölfen, H. & Antonietti, M. Mesocrystals: inorganic superstructures made by highly parallel crystallization and controlled alignment. *Angew. Chem., Int. Ed.* **44,** 5576–5591 (2005).
7 Zhou, L. & O'Brien, P. Mesocrystals: a new class of solid materials. *Small.* **4,** 1566–1574 (2008).
8 Song, R.-Q. & Cölfen, H. Mesocrystals-ordered nanoparticle superstructures. *Adv. Mater.* **22,** 1301–1330 (2010).
9 Niederberger, M. & Cölfen, H. Oriented attachment and mesocrystals: non-classical crystallization mechanisms based on nanoparticle assembly. *Phys. Chem. Chem. Phys.* **8,** 3271–3287 (2006).
10 Zhou, L. & O'Brien, P. Mesocrystals—properties and applications. *J. Phys. Chem. Lett.* **3,** 620–628 (2012).
11 Fang, J., Ding, B. & Gleiter, H. Mesocrystals: syntheses in metals and applications. *Chem. Soc. Rev.* **40,** 5347–5360 (2011).
12 Seto, J., Ma, Y., Davis, S. A., Meldrum, F., Gourrier, A., Kim, Y.-Y., Schilde, U., Sztucki, M., Burghammer, M., Maltsev, S., Jaeger, C. & Coelfen, H. Structure-property relationships of a biological mesocrystal in the adult sea urchin spine. *Proc. Natl Acad. Sci. USA* **109,** 3699–3704 (2012).
13 Zhou, L., Smyth-Boyle, D. & O'Brien, P. A facile synthesis of uniform NH_4TiOF_3 mesocrystals and their conversion to TiO_2 mesocrystals. *J. Am. Chem. Soc.* **130,** 1309–1320 (2008).
14 Liu, S.-J., Gong, J.-Y., Hu, B. & Yu, S.-H. Mesocrystals of rutile TiO_2: mesoscale transformation, crystallization, and growth by a biologic molecules-assisted hydrothermal process. *Cryst. Growth Des.* **9,** 203–209 (2009).
15 Zhang, D., Li, G., Wang, F. & Yu, J. C. Green synthesis of a self-assembled rutile mesocrystalline photocatalyst. *Cryst. Eng. Commun.* **12,** 1759–1763 (2010).
16 Ye, J.-F., Liu, W., Cai, J.-G., Chen, S., Zhao, X.-W., Zhou, H.-H. & Qi, L.-M. Nanoporous anatase TiO_2 mesocrystals: additive-free synthesis, remarkable crystalline-phase stability, and improved lithium insertion behavior. *J. Am. Chem. Soc.* **133,** 933–940 (2011).
17 Bian, Z., Zhu, J., Wen, J., Cao, F., Huo, Y., Qian, X., Cao, Y., Shen, M., Li, H. & Lu, Y. Single-crystal-like titania mesocages. *Angew. Chem., Int. Ed.* **50,** 1105–1108 (2011).
18 Tartaj, P. Sub-100 nm TiO_2 mesocrystalline assemblies with mesopores: preparation, characterization, enzyme immobilization and photocatalytic properties. *Chem. Commun.* **47,** 256–258 (2011).
19 Yu, H., Tian, B. & Zhang, J. Layered TiO_2 composed of anatase nanosheets with exposed {001} facets: facile synthesis and enhanced photocatalytic activity. *Chem. Eur. J.* **17,** 5499–5502 (2011).
20 Cai, J., Ye, J., Chen, S., Zhao, X., Zhang, D., Chen, S., Ma, Y., Jin, S. & Qi, L. Self-cleaning, broadband and quasi-omnidirectional antireflective structures based on mesocrystalline rutile TiO_2 nanorod arrays. *Energy Environ. Sci.* **5,** 7575–7581 (2012).
21 Bian, Z., Tachikawa, T. & Majima, T. Superstructure of TiO_2 crystalline nanoparticles yields effective conduction pathways for photogenerated charges. *J. Phys. Chem. Lett.* **3,** 1422–1427 (2012).
22 Chen, Q., Ma, W., Chen, C., Ji, H. & Zhao, J. Anatase TiO_2 mesocrystals enclosed by (001) and (101) facets: synergistic effects between Ti^{3+} and facets for their photocatalytic performance. *Chem. Eur. J.* **18,** 12584–12589 (2012).
23 Zhou, L., Chen, J., Ji, C., Zhou, L. & O'Brien, P. A facile solid phase reaction to prepare TiO_2 mesocrystals with exposed {001} facets and high photocatalytic activity. *Cryst. Eng. Commun.* **15,** 5012–5015 (2013).
24 Li, Z., Gessner, A., Richters, J.-P., Kalden, J., Voss, T., Kuebel, C. & Taubert, A. Hollow zinc oxide mesocrystals from an ionic liquid precursor (ILP). *Adv. Mater.* **20,** 1279–1285 (2008).
25 Liu, Z., Wen, X. D., Wu, X. L., Gao, Y. J., Chen, H. T., Zhu, J. & Chu, P. K. Intrinsic dipole-field-driven mesoscale crystallization of core-shell ZnO mesocrystal microspheres. *J. Am. Chem. Soc.* **131,** 9405–9412 (2009).
26 Wu, X. L., Xiong, S. J., Liu, Z., Chen, J., Shen, J. C., Li, T. H., Wu, P. H. & Chu, P. K. Green light stimulates terahertz emission from mesocrystal microspheres. *Nat. Nanotechnol.* **6,** 103–106 (2011).
27 Distaso, M., Klupp Taylor, R. N., Taccardi, N., Wasserscheid, P. & Peukert, W. Influence of the counterion on the synthesis of ZnO mesocrystals under solvothermal conditions. *Chem. Eur. J.* **17,** 2923–2930 (2011).
28 Distaso, M., Segets, D., Wernet, R., Taylor, R. K. & Peukert, W. Tuning the size and the optical properties of ZnO mesocrystals synthesized under solvothermal conditions. *Nanoscale* **4,** 864–873 (2012).
29 Hosono, E., Tokunaga, T., Ueno, S., Oaki, Y., Imai, H., Zhou, H. & Fujihara, S. Crystal-growth process of single-crystal-like mesoporous ZnO through a competitive reaction in solution. *Cryst. Growth Des.* **12,** 2923–2931 (2012).
30 Liu, M.-H., Tseng, Y.-H., Greer, H. F., Zhou, W. & Mou, C.-Y. Dipole field guided orientated attachment of nanocrystals to twin-brush ZnO mesocrystals. *Chem. Eur. J.* **18,** 16104–16113 (2012).
31 Sun, S., Zhang, X., Zhang, J., Song, X. & Yang, Z. Unusual designated-tailoring on zone-axis preferential growth of surfactant-free ZnO mesocrystals. *Cryst. Growth Des.* **12,** 2411–2418 (2012).
32 Waltz, F., Wissmann, G., Lippke, J., Schneider, A. M., Schwarz, H.-C., Feldhoff, A., Eiden, S. & Behrens, P. Evolution of the morphologies of zinc oxide mesocrystals under the influence of natural polysaccharides. *Cryst. Growth Des.* **12,** 3066–3075 (2012).
33 Wang, H., Xin, L., Wang, H., Yu, X., Liu, Y., Zhou, X. & Li, B. Aggregation-induced growth of hexagonal ZnO hierarchical mesocrystals with interior space: nonaqueous synthesis, growth mechanism, and optical properties. *RSC Adv.* **3,** 6538–6544 (2013).
34 Wang, S.-S. & Xu, A.-W. Template-free facile solution synthesis and optical properties of ZnO mesocrystals. *Cryst. Eng. Commun.* **15,** 376–381 (2013).
35 Park, G.-S., Shindo, D., Waseda, Y. & Sugimoto, T. Internal structure analysis of monodispersed pseudocubic hematite particles by electron microscopy. *J. Colloid Interface Sci.* **177,** 198–207 (1996).
36 Fang, X.-L., Chen, C., Jin, M.-S., Kuang, Q., Xie, Z.-X., Xie, S.-Y., Huang, R.-B. & Zheng, L.-S. Single-crystal-like hematite colloidal nanocrystal clusters: synthesis and applications in gas sensors, photocatalysis and water treatment. *J. Mater. Chem.* **19,** 6154–6160 (2009).
37 An, Z., Zhang, J., Pan, S. & Yu, F. Facile template-free synthesis and characterization of elliptic α-Fe_2O_3 superstructures. *J. Phys. Chem. C* **113,** 8092–8096 (2009).
38 Chen, J. S., Zhu, T., Li, C. M. & Lou, X. W. Building hematite nanostructures by oriented attachment. *Angew. Chem., Int. Ed.* **50,** 650–653 (2011).
39 Ma, J., Teo, J., Mei, L., Zhong, Z., Li, Q., Wang, T., Duan, X., Lian, J. & Zheng, W. Porous platelike hematite mesocrystals: synthesis, catalytic and gas-sensing applications. *J. Mater. Chem.* **22,** 11694–11700 (2012).
40 Duan, X., Mei, L., Ma, J., Li, Q., Wang, T. & Zheng, W. Facet-induced formation of hematite mesocrystals with improved lithium storage properties. *Chem. Commun.* **48,** 12204–12206 (2012).
41 Ahniyaz, A., Sakamoto, Y. & Bergström, L. Magnetic field-induced assembly of oriented superlattices from maghemite nanocubes. *Proc. Natl Acad. Sci. USA* **104,** 17570–17574 (2007).
42 He, T., Chen, D. & Jiao, X. Controlled synthesis of Co_3O_4 nanoparticles through oriented aggregation. *Chem. Mater.* **16,** 737–743 (2004).
43 Yang, H. G. & Zeng, H. C. Self-construction of hollow SnO_2 octahedra based on two-dimensional aggregation of nanocrystallites. *Angew. Chem. Int. Ed.* **43,** 5930–5933 (2004).
44 Zhuang, Z., Huang, F., Lin, Z. & Zhang, H. Aggregation-induced fast crystal growth of SnO_2 nanocrystals. *J. Am. Chem. Soc.* **134,** 16228–16234 (2012).
45 Zhao, J., Tan, R., Guo, Y., Lu, Y., Xu, W. & Song, W. SnO mesocrystals: additive-free synthesis, oxidation, and top-down fabrication of quantum dots. *Cryst. Eng. Commun.* **14,** 4575–4577 (2012).
46 Fang, J., Leufke, P. M., Kruk, R., Wang, D., Scherer, T. & Hahn, H. External electric field driven 3D ordering architecture of silver (I) oxide meso-superstructures. *Nano Today* **5,** 175–182 (2010).
47 Liu, B. & Zeng, H. C. Mesoscale organization of CuO nanoribbons: formation of "dandelions". *J. Am. Chem. Soc.* **126,** 8124–8125 (2004).
48 Yao, W.-T., Yu, S.-H., Zhou, Y., Jiang, J., Wu, Q.-S., Zhang, L. & Jiang, J. Formation of uniform CuO nanorods by spontaneous aggregation: selective synthesis of CuO, Cu_2O, and Cu nanoparticles by a solid-liquid phase arc discharge process. *J. Phys. Chem. B* **109,** 14011–14016 (2005).
49 Xu, M., Wang, F., Ding, B., Song, X. & Fang, J. Electrochemical synthesis of leaf-like CuO mesocrystals and their lithium storage properties. *RSC Adv.* **2,** 2240–2243 (2012).
50 Huang, F., Zhang, H. & Banfield, J. F. Two-stage crystal-growth kinetics observed during hydrothermal coarsening of nanocrystalline ZnS. *Nano Lett.* **3,** 373–378 (2003).
51 Yu, J. H., Joo, J., Park, H. M., Baik, S.-I., Kim, Y. W., Kim, S. C. & Hyeon, T. Synthesis of quantum-sized cubic ZnS nanorods by the oriented attachment mechanism. *J. Am. Chem. Soc.* **127,** 5662–5670 (2005).
52 Querejeta-Fernandez, A., Hernandez-Garrido, J. C., Yang, H., Zhou, Y., Varela, A., Parras, M., Calvino-Gamez, J. J., Gonzalez-Calbet, J. M., Green, P. F. & Kotov, N. A. Unknown aspects of self-assembly of PbS microscale sperstructures. *ACS Nano* **6,** 3800–3812 (2012).
53 Cho, K.-S., Talapin, D. V., Gaschler, W. & Murray, C. B. Designing PbSe nanowires and nanorings through oriented attachment of nanoparticles. *J. Am. Chem. Soc.* **127,** 7140–7147 (2005).
54 Nagaoka, Y., Chen, O., Wang, Z. & Cao, Y. C. Structural control of nanocrystal superlattices using organic guest molecules. *J. Am. Chem. Soc.* **134,** 2868–2871 (2012).
55 Fang, J., Ma, X., Cai, H., Song, X. & Ding, B. Nanoparticle-aggregated 3D monocrystalline gold dendritic nanostructures. *Nanotechnology* **17,** 5841–5845 (2006).
56 Giersig, M., Pastoriza-Santos, I. & Liz-Marzán, L. M. Evidence of an aggregative mechanism during the formation of silver nanowires in *N,N*-dimethylformamide. *J. Mater. Chem.* **14,** 607–610 (2004).
57 Fang, J., Ding, B. & Song, X. Self-assembly mechanism of platelike silver mesocrystal. *Appl. Phys. Lett.* **91,** 083108 (2007).
58 Cao, Y., Fan, J., Bai, L., Hu, P., Yang, G., Yuan, F. & Chen, Y. Formation of cubic Cu mesocrystals by a solvothermal reaction. *Cryst. Eng. Commun.* **12,** 3894–3899 (2010).
59 Yamauchi, Y., Momma, T., Fuziwara, M., Nair, S. S., Ohsuna, T., Terasaki, O., Osaka, T. & Kuroda, K. Unique microstructure of mesoporous Pt (HI-Pt) prepared via direct physical casting in lyotropic liquid crystalline media. *Chem. Mater.* **17,** 6342–6348 (2005).
60 Li, T., You, H., Xu, M., Song, X. & Fang, J. Electrocatalytic properties of hollow coral-like platinum mesocrystals. *ACS Appl. Mater. Interfaces* **4,** 6942–6948 (2012).
61 Huang, X., Tang, S., Yang, J., Tan, Y. & Zheng, N. Etching growth under surface confinement: an effective strategy to prepare mesocrystalline Pd nanocorolla. *J. Am. Chem. Soc.* **133,** 15946–15949 (2011).

62 Wohlrab, S., Pinna, N., Antonietti, M. & Cölfen, H. Polymer-induced alignment of DL-alanine nanocrystals to crystalline mesostructures. *Chem. Eur. J.* **11,** 2903–2913 (2005).
63 Medina, D. D. & Mastai, Y. Synthesis of DL-alanine mesocrystals with a hollow morphology. *Cryst. Growth Des.* **8,** 3646–3651 (2008).
64 Jiang, Y., Gong, H., Volkmer, D., Gower, L. & Cölfen, H. Preparation of hierarchical mesocrystalline DL-lysine·HCl-poly(acrylic acid) hybrid thin films. *Adv. Mater.* **23,** 3548–3552 (2011).
65 Huang, M., Schilde, U., Kumke, M., Antonietti, M. & Cölfen, H. Polymer-induced self-assembly of small organic molecules into ultralong microbelts with electronic conductivity. *J. Am. Chem. Soc.* **132,** 3700–3707 (2010).
66 Oaki, Y., Kotachi, A., Miura, T. & Imai, H. Bridged nanocrystals in biominerals and their biomimetics: classical yet modern crystal growth on the nanoscale. *Adv. Funct. Mater.* **16,** 1633–1639 (2006).
67 Fujishima, A., Zhang, X. & Tryk, D. A. TiO_2 photocatalysis and related surface phenomena. *Surf. Sci. Rep.* **63,** 515–582 (2008).
68 Chen, X., Shen, S., Guo, L. & Mao, S. S. Semiconductor-based photocatalytic hydrogen generation. *Chem. Rev.* **110,** 6503–6570 (2010).
69 Yang, Z., Zhang, J., Kintner-Meyer, M. C. W., Lu, X., Choi, D., Lemmon, J. P. & Liu, J. Electrochemical energy storage for green grid. *Chem. Rev.* **111,** 3577–3613 (2011).
70 Tachikawa, T., Fujitsuka, M. & Majima, T. Mechanistic insight into the TiO_2 photocatalytic reactions: design of new photocatalysts. *J. Phys. Chem. C* **111,** 5259–5275 (2007).
71 Liu, G., Yu, J. C., Lu, G. Q. & Cheng, H.-M. Crystal facet engineering of semiconductor photocatalysts: motivations, advances and unique properties. *Chem. Commun.* **47,** 6763–6783 (2011).
72 Zhou, K. & Li, Y. Catalysis based on nanocrystals with well-defined facets. *Angew. Chem., Int. Ed.* **51,** 602–613 (2012).
73 Yang, H. G., Sun, C. H., Qiao, S. Z., Zou, J., Liu, G., Smith, S. C., Cheng, H. M. & Lu, G. Q. Anatase TiO_2 single crystals with a large percentage of reactive facets. *Nature* **453,** 638–641 (2008).
74 Liu, S., Yu, J. & Jaroniec, M. Anatase TiO_2 with dominant high-energy {001} facets: synthesis, properties, and applications. *Chem. Mater.* **23,** 4085–4093 (2011).
75 Crossland, E. J. W., Noel, N., Sivaram, V., Leijtens, T., Alexander-Webber, J. A. & Snaith, H. J. Mesoporous TiO_2 single crystals delivering enhanced mobility and optoelectronic device performance. *Nature* **495,** 215–219 (2013).
76 Zheng, X., Kuang, Q., Yan, K., Qiu, Y., Qiu, J. & Yang, S. Mesoporous TiO_2 single crystals: facile shape-, size-, and phase-controlled growth and efficient photocatalytic performance. *ACS Appl. Mater. Interfaces* **5,** 11249–11257 (2013).
77 Park, Y., Kim, W., Monllor-Satoca, D., Tachikawa, T., Majima, T. & Choi, W. Role of interparticle charge transfers in agglomerated photocatalyst nanoparticles: demonstration in aqueous suspension of dye-sensitized TiO_2. *J. Phys. Chem. Lett.* **4,** 189–194 (2013).
78 Lakshminarasimhan, N., Bae, E. & Choi, W. Enhanced photocatalytic production of H_2 on mesoporous TiO_2 prepared by template-free method: role of interparticle charge transfer. *J. Phys. Chem. C* **111,** 15244–15250 (2007).
79 Lakshminarasimhan, N., Kim, W. & Choi, W. Effect of the agglomerated state on the photocatalytic hydrogen production with in situ agglomeration of colloidal TiO_2 nanoparticles. *J. Phys. Chem. C* **112,** 20451–20457 (2008).
80 Choi, S. K., Kim, S., Lim, S. K. & Park, H. Photocatalytic comparison of TiO_2 nanoparticles and electrospun TiO_2 nanofibers: effects of mesoporosity and interparticle charge transfer. *J. Phys. Chem. C* **114,** 16475–16480 (2010).
81 Ismail, A. A. & Bahnemann, D. W. Mesostructured Pt/TiO_2 nanocomposites as highly active photocatalysts for the photooxidation of dichloroacetic acid. *J. Phys. Chem. C* **115,** 5784–5791 (2011).
82 Tirosh, S., Dittrich, T., Ofir, A., Grinis, L. & Zaban, A. Influence of ordering in porous TiO_2 layers on electron diffusion. *J. Phys. Chem. B* **110,** 16165–16168 (2006).
83 Gonzalez-Vazquez, J. P., Morales-Florez, V. & Anta, J. A. How important is working with an ordered electrode to improve the charge collection efficiency in nanostructured solar cells? *J. Phys. Chem. Lett* **3,** 386–393 (2012).
84 Hu, B., Wu, L.-H., Zhao, Z., Zhang, M., Chen, S.-F., Liu, S.-J., Shi, H.-Y., Ding, Z.-J. & Yu, S.-H. Hierarchical silver indium tungsten oxide mesocrystals with morphology-, pressure-, and temperature-dependent luminescence properties. *Nano Res.* **3,** 395–403 (2010).
85 Bian, Z., Tachikawa, T., Kim, W., Choi, W. & Majima, T. Superior electron transport and photocatalytic abilities of metal-nanoparticle-loaded TiO_2 superstructures. *J. Phys. Chem. C* **116,** 25444–25453 (2012).
86 Tachikawa, T., Ishigaki, T., Li, J.-G., Fujitsuka, M. & Majima, T. Defect-mediated photoluminescence dynamics of Eu^{3+}-doped TiO_2 nanocrystals revealed at the single-particle or single-aggregate level. *Angew. Chem., Int. Ed.* **47,** 5348–5352 (2008).
87 Tachikawa, T., Yamashita, S. & Majima, T. Evidence for crystal-face-dependent TiO_2 photocatalysis from single-molecule imaging and kinetic analysis. *J. Am. Chem. Soc.* **133,** 7197–7204 (2011).
88 Tachikawa, T. & Majima, T. Single-molecule, single-particle fluorescence imaging of TiO_2-based photocatalytic reactions. *Chem. Soc. Rev.* **39,** 4802–4819 (2010).
89 Tachikawa, T. & Majima, T. Single-molecule, single-particle approaches for exploring the structure and kinetics of nanocatalysts. *Langmuir.* **28,** 8933–8943 (2012).
90 Jiao, W., Wang, L., Liu, G., Lu, G. Q. & Cheng, H.-M. Hollow anatase TiO_2 single crystals and mesocrystals with dominant {101} facets for improved photocatalysis activity and tuned reaction preference. *ACS Catal.* **2,** 1854–1859 (2012).
91 Liu, B. & Zeng, H. C. Carbon nanotubes supported mesoporous mesocrystals of anatase TiO_2. *Chem. Mater.* **20,** 2711–2718 (2008).
92 Yang, X., Qin, J., Li, Y., Zhang, R. & Tang, H. Graphene-spindle shaped TiO_2 mesocrystal composites: facile synthesis and enhanced visible light photocatalytic performance. *J. Hazard. Mater.* **261,** 342–350 (2013).
93 Shevchenko, E. V., Talapin, D. V., Kotov, N. A., O'Brien, S. & Murray, C. B. Structural diversity in binary nanoparticle superlattices. *Nature* **439,** 55–59 (2006).
94 Urban, J. J., Talapin, D. V., Shevchenko, E. V., Kagan, C. R. & Murray, C. B. Synergism in binary nanocrystal superlattices leads to enhanced p-type conductivity in self-assembled PbTe/Ag_2Te thin films. *Nat. Mater.* **6,** 115–121 (2007).
95 Wang, T., Zhuang, J., Lynch, J., Chen, O., Wang, Z., Wang, X., LaMontagne, D., Wu, H., Wang, Z. & Cao, Y. C. Self-assembled colloidal superparticles from nanorods. *Science* **338,** 358–363 (2012).

Takashi Tachikawa received his BS and MS in Education from Fukushima University in 1998 and 2000, respectively. He received PhD in Chemistry from Tohoku University in 2003. He worked as a postdoctoral fellow in the Institute of Scientific and Industrial Research (SANKEN), Osaka University, until 2006 and now he is working as an assistant professor.

Tetsuro Majima received his BS, MS and PhD in 1975, 1977 and 1980, respectively. He worked as a research associate in the University of Texas at Dallas (1980–1982) and as a scientist in the Institute of Physical and Chemical Research (RIKEN, 1982–1994). In 1994, he became an associate professor in SANKEN, Osaka University. He was promoted to full professor in 1997.